

High-Resolution Three-Dimensional Microelectrode Brain Mapping Using Stereo Microfocal X-ray Imaging

David D. Cox, Alexander M. Papanastassiou, Daniel Oreper, Benjamin B. Andken and James J. DiCarlo

J Neurophysiol 100:2966-2976, 2008. First published 24 September 2008; doi:10.1152/jn.90672.2008

You might find this additional info useful...

This article cites 15 articles, 4 of which can be accessed free at:

<http://jn.physiology.org/content/100/5/2966.full.html#ref-list-1>

This article has been cited by 1 other HighWire hosted articles

In vivo visualization of single-unit recording sites using MRI-detectable elgiloy deposit marking

Kenji W. Koyano, Akinori Machino, Masaki Takeda, Teppei Matsui, Ryoko Fujimichi, Yohei Ohashi and Yasushi Miyashita

J Neurophysiol, March , 2011; 105 (3): 1380-1392.

[\[Abstract\]](#) [\[Full Text\]](#) [\[PDF\]](#)

Updated information and services including high resolution figures, can be found at:

<http://jn.physiology.org/content/100/5/2966.full.html>

Additional material and information about *Journal of Neurophysiology* can be found at:

<http://www.the-aps.org/publications/jn>

This information is current as of June 2, 2011.

High-Resolution Three-Dimensional Microelectrode Brain Mapping Using Stereo Microfocal X-ray Imaging

David D. Cox,^{1,2} Alexander M. Papanastassiou,¹ Daniel Oreper,¹ Benjamin B. Andken,¹ and James J. DiCarlo¹

¹McGovern Institute for Brain Research and Department of Brain and Cognitive Sciences, Massachusetts Institute of Technology; and ²The Rowland Institute at Harvard, Harvard University, Cambridge, Massachusetts

Submitted 12 June 2008; accepted in final form 15 September 2008

Cox DD, Papanastassiou AM, Oreper D, Andken BB, DiCarlo JJ. High-resolution three-dimensional microelectrode brain mapping using stereo microfocal X-ray imaging. *J Neurophysiol* 100: 2966–2976, 2008. First published September 24, 2008; doi:10.1152/jn.90672.2008. Much of our knowledge of brain function has been gleaned from studies using microelectrodes to characterize the response properties of individual neurons in vivo. However, because it is difficult to accurately determine the location of a microelectrode tip within the brain, it is impossible to systematically map the fine three-dimensional spatial organization of many brain areas, especially in deep structures. Here, we present a practical method based on digital stereo microfocal X-ray imaging that makes it possible to estimate the three-dimensional position of each and every microelectrode recording site in “real time” during experimental sessions. We determined the system’s *ex vivo* localization accuracy to be better than 50 μm , and we show how we have used this method to coregister hundreds of deep-brain microelectrode recordings in monkeys to a common frame of reference with median error of <150 μm . We further show how we can coregister those sites with magnetic resonance images (MRIs), allowing for comparison with anatomy, and laying the groundwork for more detailed electrophysiology/functional MRI comparison. Minimally, this method allows one to marry the single-cell specificity of microelectrode recording with the spatial mapping abilities of imaging techniques; furthermore, it has the potential of yielding fundamentally new kinds of high-resolution maps of brain function.

INTRODUCTION

The use of extracellular microelectrodes to record action potentials in vivo has been a staple technique of neurophysiology for the last four decades. However, although microelectrodes offer exquisite single-cell specificity, each electrode can record from only one or a few cells at a time and populations of cells are typically sampled serially, over the course of many sessions. To develop spatial maps of cell properties, the three-dimensional (3D) locations of recorded cells must somehow be resolved across these many sessions. However, the position of a microelectrode can be known accurately only before it is inserted into the brain, after which the experimenter is “blind” to the electrode’s trajectory and must typically rely on extrapolation. This fact has practically limited fine-grained microelectrode mapping to superficial structures, near the skull surface, since extrapolative uncertainty, while still present, is bounded by the short distances traveled.

However, many brain structures of interest (e.g., subcortical structures, ventral cortex) are located deep within the brain and

cannot be accessed directly from the skull surface. Performing fine-grained mapping of such structures is problematic because electrodes must travel large distances to reach their target and even small errors in alignment at the electrode insertion point can produce large position errors at the depth. For instance, at a depth of 40 mm (typical for recordings from ventral inferior temporal cortex of nonhuman primates), just a 2° angular error at the surface will produce a >1-mm displacement in the target brain structure. Such effects are compounded by the desire to use thinner microelectrodes (to minimize tissue damage), which are inherently more flexible, and thus less guaranteed to travel straight. In general, given these factors, “dead reckoning” of electrode target position from insertion geometry cannot be done with high accuracy and our knowledge of the fine-scale organization of deep structures is consequently limited.

The decades-old neurophysiology “gold standard” method for localizing microelectrode recording sites is the electrolytic microlesion—electrical current is used to produce tissue damage at the tip site that can be observed postmortem. Although useful, this method has severe limitations: it damages the tissue of interest, is very labor intensive, and has limited accuracy, especially in 3D (because lesions can be >200 μm , are often irregular in shape, and because tissue must be fixed and cut). Most critically, the method allows only a very limited number of sites within a local region to be reconstructed (~10) and only postmortem. The recent use of microelectrode coating dyes (DiCarlo et al. 1996; Naselaris et al. 2005; Snodderly et al. 1995) in combination with microdrive depth readings can avoid tissue damage and enhance the number of sites recovered (~100), but still incurs the other limitations of microlesions. Some existing imaging modalities can be used on-line and thus can, in principle, allow the reconstruction of an unlimited number of sites. However, these either have limited accuracy (ultrasound; Glimcher et al. 2001) or are costly, labor intensive, and not practical for everyday use (magnetic resonance imaging [MRI] with electrodes in place; Matsui et al. 2007; or following iron deposition; Fung et al. 1998). Extrapolation methods (e.g., frameless stereotaxy), although useful for some surgical procedures, have limited accuracy because small errors are amplified in the process of extrapolation, especially in deep brain structures (as described earlier).

X-rays represent an attractive alternative technology for localizing microelectrodes because electrode materials are typically much more X-ray opaque than biological tissue and because X-ray sources and detectors are commercially avail-

Address for reprint requests and other correspondence: J. J. DiCarlo, McGovern Institute for Brain Research and Department of Brain and Cognitive Sciences, Massachusetts Institute of Technology, Cambridge, MA 02139 (E-mail: dicarlo@mit.edu).

The costs of publication of this article were defrayed in part by the payment of page charges. The article must therefore be hereby marked “advertisement” in accordance with 18 U.S.C. Section 1734 solely to indicate this fact.

able, inexpensive, and robust. Nahm and colleagues (1994) previously described a method based on X-ray stereophotogrammetry to localize microelectrodes during an experiment. In this technique, two X-ray radiographs were taken serially from two vantage points with an electrode in the brain. By locating the microelectrode on each of the resulting X-ray films, the electrode tip position could be triangulated. Additionally, fiducial markers with both X-ray and MRI contrast were affixed to the skull and triangulating these objects allowed coregistration of the X-ray and MR images. However, although the described system was very promising, it had several drawbacks. For one, images were acquired serially, requiring greater operator intervention and increasing the odds that the subject was able to move slightly between acquisitions. The system was also film-based, requiring substantial off-line processing to produce a microelectrode position estimate. In addition, a standard X-ray source with a large focal spot was used, limiting the maximum achievable definition possible in the images. Finally, although the authors demonstrated the system in use, they did not provide a systematic, quantitative analysis of typical accuracy, instead stating that the system accuracy was limited by MRI voxel size, at 625 μm .

Here, we extend this work, building a system based on a pair of microfocal X-ray sources and digital X-ray detectors, with the goal of producing highly accurate, rapid, “real-time” estimates of microelectrode position during an experimental session. Because images can be collected quickly and without interrupting ongoing electrophysiology, we were able to acquire X-ray-based microelectrode tip position estimates of every one of several hundred recording sites over the course of a standard electrophysiological experiment. We argue that this approach opens up new potential for high-resolution physiological 3D mapping of brain activity in awake, behaving animals.

METHODS

Animals

Two rhesus macaque monkeys were used in this study (although all data, with the exception of skull/dura collision data presented in Fig. 7, were taken from one animal). Aseptic surgery was performed to implant a head post and recording chamber (targeting inferior temporal cortex). Animal training, surgical procedures, eye monitoring, and recording methods were performed using standard techniques for awake, primate visual neurophysiology (e.g., Zoccolan et al. 2005). Because these animals also underwent functional magnetic resonance imaging (fMRI), head-post implant materials were modified to be MR-compatible (Op de Beeck et al. 2008) and eye tracking was done using a video-based system (EyeLink II, SR Research), but these modifications are not required for use of the microelectrode localization method presented here. All procedures were done in accordance with the MIT Committee on Animal Care.

Microelectrode recording

Single microelectrode recordings were performed using standard awake monkey visual physiology techniques (Zoccolan et al. 2005). Glass-coated tungsten microelectrodes (total outer diameter, 310 μm ; tungsten shank diameter, 150 μm ; length, 130 mm; taper angle, 60°; 0.2–0.3 M Ω ; Alpha Omega) were used to record neuronal activity. On each recording day, a single electrode was advanced through a guide tube (~15 mm into tissue) placed in a selected grid location. A hydraulic microdrive (Kopf Instruments) was used to advance the electrode and recordings were made at a series of sites in the temporal

lobe (10–30 mm of travel beyond the guide tube), typically with a depth separation of 200–500 μm between each site. The microdrive depth reading was recorded at each recording site and used as a means of validating X-ray position estimates (see RESULTS, Fig. 6). To ensure the accuracy of microdrive readings, the hydraulic fluid was routinely refilled and the drive was monitored for signs of leakage. X-ray imaging (see following text) was performed at each recording site.

For the physiological data reported here, the animal performed a simple visual fixation task during which visual stimuli were rapidly presented (as in Zoccolan 2005). Multiunit activity was collected by placing a hardware threshold at approximately 2 standard deviations above the background voltage fluctuations recorded on the electrode and each crossing of that threshold was counted as a multiunit “event” (see Kreiman et al. 2006 for details). The multiunit threshold was set on each day (i.e., each microelectrode penetration) and was held constant for the entire recording session.

X-ray system

A pair of X-ray images was acquired at each recording site using two microfocal X-ray sources (Apogee 5000, 50 kV, 1 mA, ~35- μm focal spot, tungsten target; 0.5-mm aluminum filter; Oxford Instruments), each projecting its beam onto a 1-megapixel CCD X-ray camera (Shad-o-Snap 1024 with Remote RadEye2 EV, Premium Grade, Min-R scintillator, pixel width $\approx 50 \times 50 \mu\text{m}$; 50 \times 50-mm field of view [FOV]; Rad-icon Imaging). The overall system layout is shown in Figs. 1A and 2. The source–detector pairs were affixed to a custom-built gantry that held the sources and detectors from above (no X-ray image occlusion). This gantry allowed the entire apparatus to be lowered, translated, and rotated around the animal’s head and also allowed each source–detector pair to rotate independently around a common center point (and then be fixed in place). The two source–detector pairs were rotated (and then fixed) such that the “spread” angle between them was as close to 90° as possible (an angle of ~60° was used here), while ensuring that both pairs had a “clear shot” of the microelectrode and external fiducial markers (see following text) and that the source–detector pairs minimally occluded the visual field of the animal (for the experiments reported here, FOV was approximately $\pm 15^\circ$ with the system in place). Once rotation spread was determined and fixed, the system was calibrated (see following text) and could then be repositioned each day using four degrees of freedom (df; translation and system rotation) without need for further calibration (see RESULTS). Figure 2 shows how the system was physically arranged in an existing physiology setup.

The use of small focal spot X-ray sources enabled relatively sharper images than traditional X-ray sources, and the X-ray strength was chosen to produce reasonably high contrast images while limiting the animal’s long-term X-ray exposure to an acceptable level. Images were acquired simultaneously by both source–detector pairs, with an integration time of 4 s. This integration time represents a trade-off between increased image quality through time averaging of incoming X-ray flux, balanced against the probability of the animal moving slightly during acquisition (see DISCUSSION). Under computer control, the X-ray sources were electrostatically “shuttered,” using the X-ray tube’s focus terminal to deflect electrons away from the tube’s anode target, allowing precise on–off control over total X-ray exposure.

The total system cost was approximately \$40,000, not including machining/labor costs. The most significant components of this cost are the X-ray sources (~\$6,000 each) and the X-ray detectors (~\$13,000 each). Because the system is filmless, its operation costs are negligible. A bill of materials is available at <http://www.x-runner.org>, along with other information and materials regarding this system.

X-ray safety

Human operator and animal safety were ensured in consultation with MIT’s Radiation Safety Office. The X-ray beam cone was

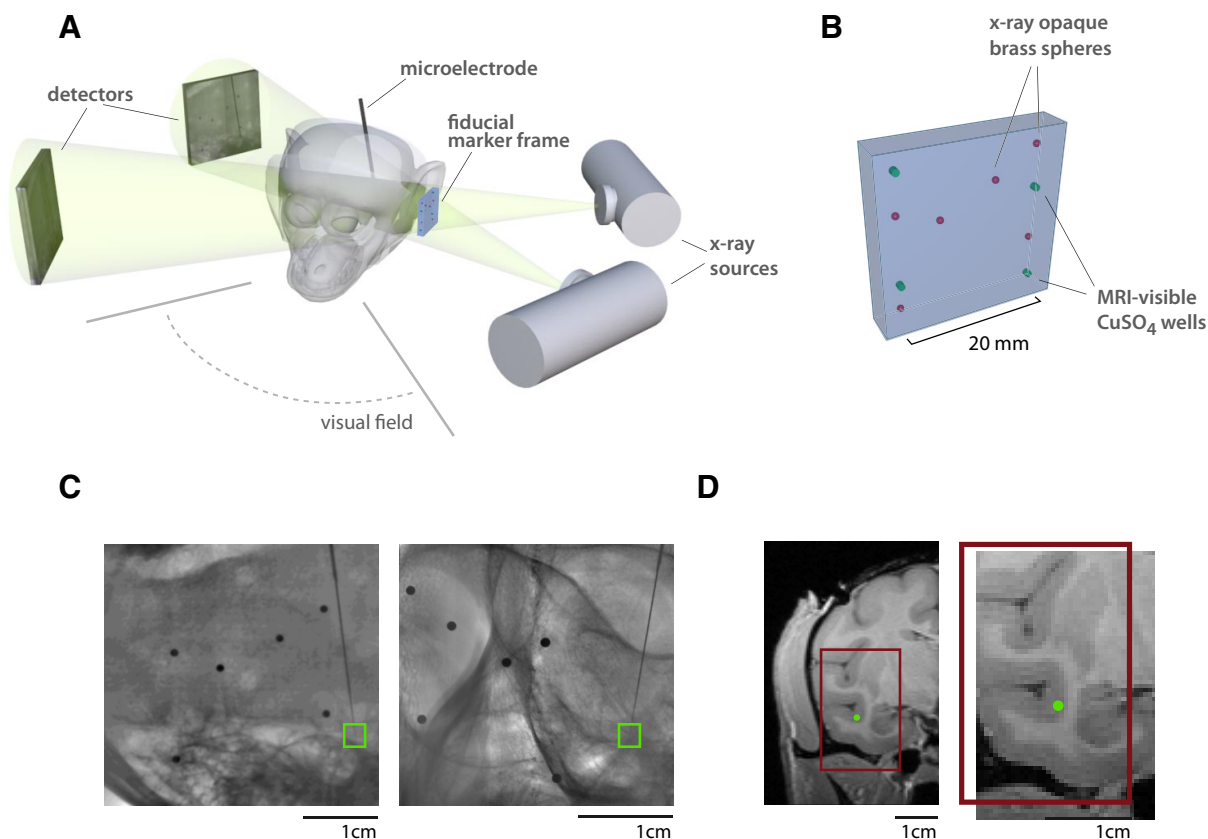


FIG. 1. A stereo microfocal X-ray 3-dimensional (3D) imaging system. **A:** basic system layout. A pair of X-ray sources project X-rays through a region containing a recording microelectrode (not shown to scale), onto a pair of digital X-ray detectors. The X-ray source/detectors are all fixed relative to each other (during operation) and are arranged such that their angular separation is as large as possible, while still allowing a mostly unobstructed visual field. A plastic fiducial marker frame containing X-ray-opaque metal fiducial spheres is additionally mounted to the animal's head post, alongside the head in the path of the X-ray beams. For presentation purposes, the figure shows one possible configuration, but this does not exactly match the spatial layout used to obtain the data presented in this study. **B:** a schematic showing the positions of X-ray-opaque brass spheres and magnetic resonance imaging (MRI)-visible CuSO₄-filled wells in the fiducial marker frame used in this study. The known arrangement of these X-ray- and MRI-visible markers allows coregistration of these 2 modalities. **C:** an example image pair produced by the X-ray system. The 6 dark circles on each image are the shadows cast by 1-mm-diameter fiducial spheres in a fixed, skull-based external reference frame (see **A** and METHODS). The dark line to the right of each image is the microelectrode shadow (green squares indicate the region around the tip). The wavy dark regions in the background reflect different amounts of X-ray attenuation by the bony structure of the skull. Bars indicate scale at the depth plane at the center of the target imaging volume. **D:** stereo images allow for the reconstruction of the 3D locations of points visible in both images. 3D points can in turn be coregistered with MR images, by using fiducial objects that include both X-ray- and MR-visible markers (see METHODS). The green dot shows the tissue location of the electrode tip measured in **C**.

approximately matched to the size of the detector plate, so that little of the direct beam escaped the space between the sources and detectors, and lead curtains were placed around the sides of the monkey setup (Fig. 2) behind the detectors as an added precaution against operator exposure from stray X-rays. Our existing monkey setups were additionally already contained with separate "cubicle" rooms (made of drywall, with a standard steel door) and the wallboard and doors in these rooms were already sufficient to reduce exposure to undetectable levels so that no additional room shielding was needed. The X-ray sources and detectors were always operated from outside the cubicle room with the door closed. As a double check, radiation safety badges were placed at fixed locations inside and outside the cubicle room and checked every 3 mo. The measured additional dosing inside the cubicle room averaged only about 0.8 mSv per year during peak usage periods (for comparison, humans naturally receive 1 to 3.6 mSv per year; Bashore et al. 2001; Clarke et al. 1989). To put this in perspective, if a person had been standing in the cubicle room (i.e., a few feet from the animal) for an entire year of active system use (neither needed nor recommended), he or she would have received only slightly more additional dosing than a frequent flyer (~0.4 mSv) and less than an airline pilot (Clarke et al. 1989). No radiation dosing above background was found at any

tested location outside the room (i.e., no extra radiation at any human locations).

The biggest short-term (nonstochastic) risk to research animals in this system is the potential for skin burning (similar to a sunburn due to absorption of some X-rays at the skin locations facing the sources). For the system configuration used to collect the data reported here, the system delivered about 0.01 Gy to the skin per X-ray image pair acquisition. If 10 such acquisitions are taken per day, the total monthly skin dosing (~2 Gy) is less than that which can be used safely in (single-day) human X-ray diagnostic procedures such as fluoroscopy-guided catheterization (Vlietstra et al. 2004). Further optimizations such as thicker source filters (we used a 0.5-mm Al filter) would further harden the X-ray beam (higher fraction of high-energy X rays), which could allow useful images to be acquired with even lower skin risk. Over the course of the experiments presented here (peak usage of 250 acquisitions/mo), no signs of skin erythema or other morbidity were observed in either animal.

External fiducial markers

To provide a common 3D reference frame across sessions, a specially constructed fiducial marker panel (4.5 × 4.0 cm, 6 mm

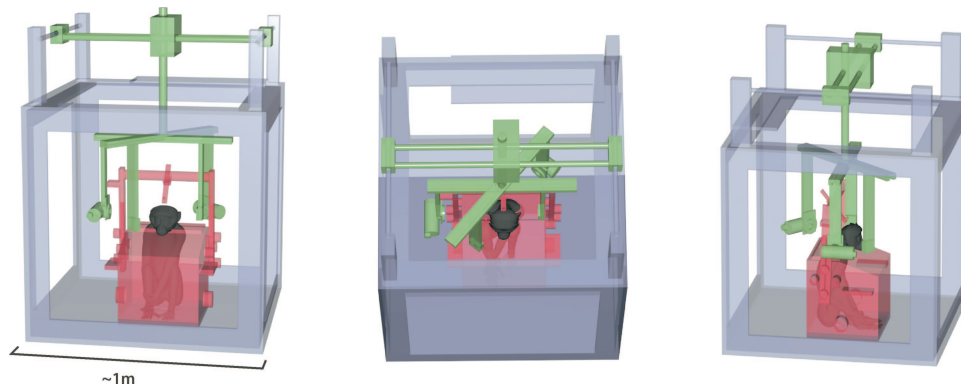


FIG. 2. Three views of the spatial layout of the system as it is installed in an existing awake monkey physiology setup. The existing frame surrounding the subject is shown in gray, the primate chair/carrier is shown in red, and X-ray system components are shown in green. The X-ray gantry holds 2 X-ray source–detector pairs, with each source always maintained in alignment with its detector (i.e., the center line of the X-ray cone is approximately normal to the detector plane and approximately intersects its center). The design allowed changes in: the angle between the 2 source–detector pairs, the distance of each source from the target, and the distance of each detector from the target (while maintaining source–detector alignment). The images above reflect just one possible configuration. The total outside physical “envelope” of the system was about 60 cm, which was easily contained inside our 1-m scleral search coil setup (gray). After locking in such changes at the first day of recording in each animal, the system was recalibrated (see METHODS). The design included an overhead crank (not shown) that allowed the arms holding the X-ray apparatus to be lifted up and out of the way (vertical translation), to facilitate the insertion and removal of the animal chair. The apparatus could also be translated in the horizontal plane and rotated around its vertical axis to optimize the X-ray images (e.g., avoid interference by components of the chair) and optimize the monkey’s visual field of view (the visual stimulus display monitor sat just outside the front end of the setup, not shown here). All 4 of these degrees of freedom were utilized daily without the need to recalibrate the system (see METHODS) and with little effect on system stability (see RESULTS).

thick) was constructed so that, at the start of each recording session, the panel could be reproducibly placed alongside the animal’s head by attachment to the head-post implant (i.e., fixed in a skull-based reference frame). This panel was constructed from plastic (polyether-imide). It was machined such that six, 1-mm-diameter brass spheres (Brass; $1 \pm 25.4 \mu\text{m}$; Grade 200; Bal-tec) were permanently fixed into holes spaced along the surface of the panel (X-ray–visible fiducial markers) and four 2×2 -mm cylindrical wells along the surface of the panel were filled with a CuSO_4 solution (MR-visible fiducial markers). The precise 3D relationship of these fiducials was needed to accurately project 3D locations into MR volumes (see RESULTS), which was determined using off-site, microcomputed tomography (micro-CT) of the marker panel (Micro Photonics, Allentown, PA) before the experiments began.

Standard workflow

An outline of the standard workflow for our system is shown in Fig. 3. The system is periodically calibrated, using a known standard “calibration object,” to precisely estimate the internal system geometry (see following text). When an electrode is positioned in the brain and its 3D tip location is desired, the following steps are performed by the system. 1) Image acquisition: two images (one from each detector) are simultaneously acquired. 2) Image segmentation: corresponding features (fiducial sphere centers and microelectrode tip) are located in each X-ray image. 3) 3D reconstruction: 3D positions of each object

(fiducial centers and microelectrode tip) are computed in the native system reference frame using the system’s internal geometry determined during calibration. 4) The microelectrode 3D tip position is projected into the common, fiducial-based reference frame (e.g., a skull-based reference frame Fig. 1B). 5) Optional coregistration to other imaging modalities is done using rigid 3D transforms (e.g., to an anatomical MRI image to establish tissue-relative mapping). Images, 3D coordinates, and MRI-coregistered position estimates are displayed to the user for real-time use (e.g., to guide immediate action during a recording session) and stored for off-line analysis.

IMAGE ACQUISITION. Two X-ray images (one from each detector) were simultaneously acquired via remote operation outside the recording room by sequentially: powering both X-ray sources (ramping over several seconds), electrostatically shuttering both sources to be open (emitting x-rays), integrating the detector arrays simultaneously (typically 4 s), shuttering both sources to be closed, and powering down both X-ray sources (ramping). The pair of acquired images was immediately transmitted to a host computer over universal serial bus. The entire acquisition process could be completed in <10 s (see DISCUSSION).

IMAGE PROCESSING AND SEGMENTATION. Gains and offset values were applied to each image pixel based on initial detector sensitivity calibration. Image features (e.g., the microelectrode tip) were then located in each X-ray image pair. For this study, the (x, y) coordinates of the fiducial spheres and the microelectrode tip were located in each

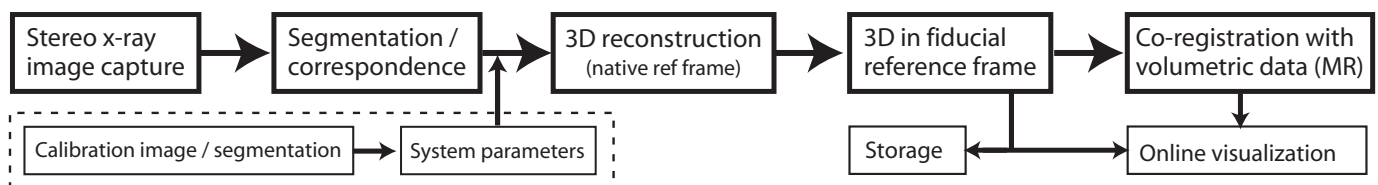


FIG. 3. Standard system work flow. 1) Stereo X-ray images are simultaneously captured under computer control. 2) Image features (corresponding fiducial centers and the microelectrode tip) are located in each image. 3) These image locations, along with previously computed system parameters (e.g., relative positions and orientations of the system components), are combined to locate each feature in the native reference frame of the system. 4) The 3D location of the microelectrode tip is then specified in a common reference frame established by the 3D locations of the fiducial markers (the “fiducial reference frame”—skull-based in this study). 5) At this point, 3D coordinates can be stored for off-line analysis or can be immediately visualized relative to structural and/or functional MR images by transforming them into the reference frame of a previously acquired structural MR image (see marker frame in Fig. 1 and METHODS). The system must be calibrated once at the beginning of use and recalibrated only if the internal system geometry is changed (dashed box; see METHODS).

image by an experimenter using an in-house, graphical user assist tool; in principle, this step could also be performed using appropriate machine vision techniques (see DISCUSSION). In this work, correspondences between the fiducial projections in each image were selected manually, although this step could, in principle, be done automatically.

3D RECONSTRUCTION IN NATIVE SYSTEM REFERENCE FRAME. Three-dimensional coordinates of all relevant objects (fiducial sphere centers and electrode tip) were found using standard stereophotogrammetry techniques (Valstar et al. 2002). Briefly, the 3D location of a target was found by computing the best-fit point to the intersection of the rays projecting from each source to the corresponding locations of the feature on each X-ray detector panel. Given the 3D location of the X-ray focal spot (s), the center of the detector panel (d), the unit-length vector normal to the plane of the X-ray detector panel (n), and a known 3D target object location (t ; e.g., the center of a small, spherical fiducial), the image of the target will project onto the detector panel at the 3D point P , where

$$P = s + \left(\frac{n \cdot (d - s)}{n \cdot (t - s)} \right) (t - s) \quad (1)$$

This point P can be straightforwardly projected into the 2D space of the detector imaging plane, given the 3D location of the upper left corner of the detector panel (u), and the orthonormal column vectors defining the row (r) and column (c) directions of the sensor panel

$$P' = \begin{bmatrix} r \cdot (P - u) \\ c \cdot (P - u) \end{bmatrix} \quad (2)$$

where the elements of P' are the (x, y) coordinates of the target point.

Given the preceding equations, one can construct a “forward” projection function $F(t, G)$ that maps the 3D target object position (t) and a collection of parameters describing the system geometry for both source detector pairs (G) onto the vector of image coordinates in both detector panels

$$F(t, G) = \begin{bmatrix} P'_1 \\ P'_2 \end{bmatrix} \quad (3)$$

where P'_1 and P'_2 are the (x, y) coordinates of the image of the target point on the first and second detector panels, respectively.

Thus the 3D position of the target point can be estimated by finding the least-squares solution for t in Eq. 3, given both the system geometry G (see following text), and the measurements of P'_1 and P'_2 taken from the first and second X-ray images, respectively. In the present work, the Levenberg–Marquardt algorithm was used to perform this optimization and a stable solution was typically found in <10 iterations.

3D RECONSTRUCTION IN FIDUCIAL-MARKER–BASED REFERENCE FRAME. By measuring 3D positions of at least three noncollinear, rigidly arranged fiducial markers, it was straightforward to define a standard reference frame and to project all microelectrode tip position estimates into this frame. For the data collected in this study, the fiducial-marker reference frame was external to the animal and rigidly affixed to the skull (see external fiducial markers in previous text). Thus all microelectrode positions (across recording time within a day or across separate recording days) were reconstructed in a common, skull-based reference frame (the external fiducial reference frame). Internal, tissue-based fiducial reference frames are also possible using the same methods (see DISCUSSION).

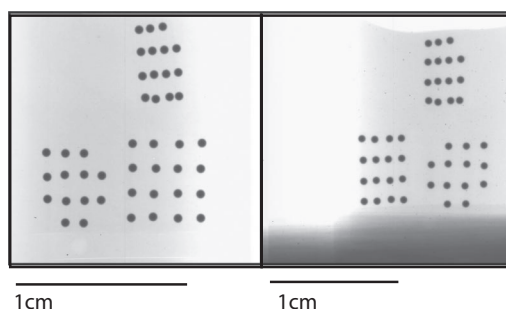
COREGISTRATION TO OTHER IMAGING MODALITIES. In principle, microelectrode locations can be determined in any volumetric data that can be coregistered with the X-ray–visible fiducial reference frame (above). In this study, we coregistered to anatomical MRI data. To do this, an anatomical MRI volume (MPRAGE, $448 \times 448 \times 160$, 500- μ m isotropic voxels; FOV = 224; Siemens Trio Tim 3T; custom-built surface coil) was acquired of the animal’s head with the fiducial panel

(described earlier) affixed to the animal’s head post (same as during the microelectrode recording sessions). Copper sulfate wells in the fiducial panel produced bright spots on the MRI, establishing an MR–fiducial frame. Given the known (via micro-CT, above) 3D relationship of the (rigid) MR–fiducial reference frame (CuSO₄ wells) and the (rigid) X-ray–fiducial reference frame (brass spheres), microelectrode positions in the fiducial reference frame were simply projected into the MR volume using the appropriate rigid-body transformation.

System calibration

System geometry (G in Eq. 3) was precisely determined by imaging a calibration object and system accuracy was measured using a validation object. Both objects were specially fabricated: they consisted of stainless steel spheres (series 440C stainless; $508 \pm 2.54 \mu\text{m}$, Grade 25; Bal-tec) embedded in a low-temperature coefficient, X-ray–transparent epoxy resin (Epotek 301; Epoxy Technology, Billerica, MA), with the calibration object containing 44 spheres and the validation object containing 6 spheres. The objects were volumetrically imaged off-site using micro-CT (Micro Photonics). The validation object was roughly $6.0 \times 5.4 \times 7.3 \text{ mm}$ and the calibration object was roughly $6.9 \times 10.1 \times 11.9 \text{ mm}$ in size (see Fig. 4), approximating the target imaging volume in the monkey, although this is not required. The known arrangement of fiducial spheres in the calibration object were used in combination with X-ray images of the object to precisely estimate parameters of the internal spatial geometry of the system. In analogy to the solution for 3D target location given known system geometry described earlier (Eq. 3), system geometric parameters (G) were estimated by solving the comparable system of equations for unknown system geometry, given (all 44) known target locations.

A Calibration Object



B Validation Object

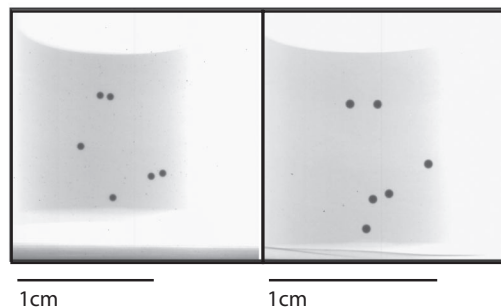


FIG. 4. Stereo pairs of X-ray images of specially fabricated test objects used for periodic calibration of system parameters (e.g., system geometry) and validation of system performance. A: calibration object (44 fiducial markers). B: validation object (6 fiducial markers). Black dots are shadows of spherical, stainless steel spheres (fiducials) embedded in epoxy (see METHODS). Bars indicate scale at the depth plane at the center of the object.

The calibration object was imaged any time that any part of the internal system geometry was changed (e.g., if the angle between the two source–detector pairs changed). Note that calibration was not needed if the entire system was moved as a single unit (4 df to reposition the system around the animal; see X-ray imaging in the previous text) because this left the internal system geometry (G) nominally unchanged. Calibration was performed approximately once a month, to guard against accidental perturbations of system geometry (although see RESULTS for data on calibration stability).

In all, 12 parameters are needed to fully define the internal system geometry (G): 18 parameters to define two point X-ray sources and two objects (detector arrays) in an external (e.g., room-based) reference frame (minus 6 parameters when the reference frame is specified internally). For clarity, those 12 values are not reported here. However, to give a sense of the system geometry based on such calibration: the distance from the sources to detectors was about 425 mm (pair 1: 399.46 mm; pair 2: 453.51 mm), the spread angle between the two source–detector lines was 59.1° and the approximate magnification of the center of the target imaging area (crossing point of the source–detector lines) was $\times 1.39$ (source–detector pair 1) and $\times 1.71$ (source–detector pair 2).

System validation

To test system *ex vivo* performance, stereo X-ray images were taken of the validation object (see preceding text) and the 3D locations of all six fiducial spheres were reconstructed (as described earlier). To obtain accuracy measurements that were comparable to the intended *in vivo* use, one of the six fiducial spheres was treated as the “microelectrode” and the others were treated as the fiducial reference frame (all combinations were considered in this manner), and the known 3D relative locations of the fiducial spheres (known via micro-CT, above) were used to compute accuracy (see RESULTS).

RESULTS

Ex vivo accuracy and stability

As a first step in determining the accuracy of our 3D X-ray imaging system, we conducted a series of *ex vivo* tests designed to assess the limits on the system imposed by imaging resolution, X-ray focal spot size, and stability of system ge-

ometry (e.g., stability of the spatial arrangement of the X-ray sources, relative to the detectors). A specially created validation object containing six stainless steel spheres (see METHODS) was volumetrically imaged offsite using micro-CT (Micro Photonics) with a resolution of about $5\ \mu\text{m}$ and these micro-CT–derived measurements served as ground truth for the comparisons that follow. The validation object was imaged using our system and the 3D locations of each sphere in the validation object were independently estimated (see METHODS). To compare these estimates with the micro-CT data, a subset of the sphere center position estimates (three, four, or five spheres) was first used to determine an optimal rigid transformation between the micro-CT reference frame and the native (internal geometry) reference frame of our system. The remainder of the sphere center position estimates were then projected into the micro-CT reference frame and errors were computed between the projected estimate and the ground-truth position (error was measured as absolute 3D distance). Figure 5A shows a summary of the position errors measured by this procedure. In all cases, our system produced highly accurate position estimates, with median error $<30\ \mu\text{m}$ and 95% of errors $<60\ \mu\text{m}$.

To test the stability of system calibration across time, the calibration and validation objects were imaged approximately once a month over the course of development and daily animal use (221 days). In addition to providing a check that the accuracy described in the preceding paragraph is reproducible across many months, this procedure also allowed the assessment of the stability of the calibration over time because the validation object could be studied using system calibrations determined in previous sessions (e.g., the validation object images from month 4 can be processed using system parameters calibrated from month 1, month 2, etc.). System accuracy (compared against micro-CT) as a function of time since last calibration is shown in Fig. 5B. Median errors are consistently $<30\ \mu\text{m}$, irrespective of time, indicating that the system remains accurate to a few tens of microns, even with infrequent recalibration and months of use.

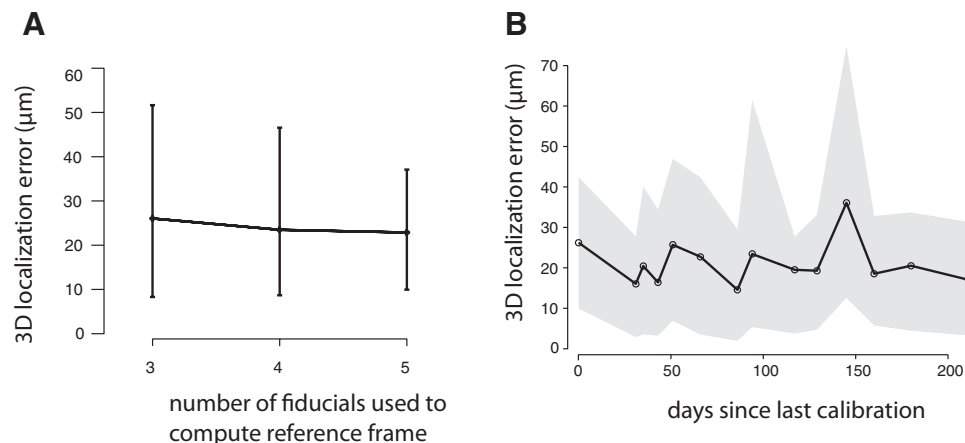


FIG. 5. *Ex vivo* validation. *A*: median system 3D localization errors imaging as a function of the number of fiducial spheres used to compute a reference frame. Values reflect absolute 3D distance of estimated “microelectrode tip” location and true location (based on micro-CT; see RESULTS). Error bars show 5 and 95% quantiles. Accuracies better than $50\ \mu\text{m}$ are routinely achievable, even with only a few fiducial spheres establishing a frame of reference. *B*: median system stability as a function of time (days) since calibration (black line). Gray area shows the region from the 5 to 95% quantiles. In general, system accuracy is stable across many days, even when the calibration is not performed regularly. Tests with the same validation object images, but using different system calibrations, show a similar pattern of error (i.e., slightly larger on the same days where error is slightly larger in *B*), suggesting that validation object imaging error—though very small—is a larger source of error than system calibration error (data not shown).

In vivo measurements

To characterize the properties of the X-ray system in practice, we used it to localize 3D microelectrode positions over the course of a standard primate visual electrophysiology experiment. Serial multiunit recordings were made at 228 sites in the temporal lobe, across 20 separate microelectrode penetrations. At each recording site, an X-ray image pair was acquired and the 3D position of the microelectrode was computed (see METHODS). Figure 6A shows all 228 recording sites registered into a common reference frame (external, skull-based fiducial reference frame; see METHODS). A volume-rendered, coregistered structural MRI image is overlaid in Fig. 6B to provide anatomical bearings.

Beyond the *ex vivo* accuracy reported earlier, several additional factors, in practice, limit system accuracy in its intended usage *in vivo*. For one, X-ray shadows produced by inhomogeneities in the bone of the skull add “noise” to the image. Second, microelectrodes taper to a very fine point, often just a few tens of microns wide at the tip. Because the microelectrode tip is small relative to the focal spot of the X-ray source (35 μm), it primarily casts a partial shadow (penumbra), rather than a complete one (umbra), smearing its image over space and lowering its contrast. Consequently, these features are at the extreme edge of the resolution of the system and can be difficult to locate consistently, particularly if there is a substantial amount of noise present in the image.

To begin to quantify these factors, we compared X-ray-derived sequential depth estimates to those obtained from the microdrive used to advance the microelectrode. Although microdrive-derived estimates are not especially useful for determining absolute 3D position (e.g., because of the effect of angular errors described in the INTRODUCTION), such measurements are nonetheless quite accurate for the measurement of depth along the microelectrode track. The stepper motor associated with the hydraulic microdrive used here is accurate to $\geq 1 \mu\text{m}$ and, leaving aside the possibility that the microelectrode curves slightly within the brain and possible errors due to the hydraulics themselves (e.g., leakage, thermal expansion), we here take these microdrive-derived depth measurements to be ground truth.

To compare X-ray-based depth measurements to microdrive-based measurements, a 3D line was fit to the position estimates for the sequence of recording sites along each microelectrode penetration. X-ray-based position estimates were then each decomposed into a depth component (in the direction along the microelectrode track) and a lateral component (absolute deviation from the fit line; Fig. 7A). Since microdrive depth readings are inherently relative (there is no clear “zero” point), the mean was subtracted from the microdrive-derived depth measurements and the mean of the X-ray-derived depth estimates was added, bringing the two sets of estimates into a common frame of reference.

Lateral errors were quite small, with a median deviation of 52.7 μm and with 95% of sites having errors $< 177.3 \mu\text{m}$ (Fig. 7B). Disagreements between X-ray- and microdrive-derived depth estimates were somewhat larger, with a median error of 136.2 μm and 95% of errors $< 481.3 \mu\text{m}$ (Fig. 7, C and D). Larger errors in depth estimates are likely due to errors in locating the microelectrode’s fine tip in images as it passed through regions of greater interference from bony structures.

Comparison with anatomy

DURA/BONE COLLISIONS. At the end of a few recording sessions, the microelectrode was purposely driven beyond audibly active brain tissue, just into the dura/bone beneath the ventral surface of the temporal lobe. Such dura/bone collisions can provide a rough check on microelectrode depth, since driving a microelectrode into dura mater or bone damages the microelectrode tip, producing a characteristic “crunching” noise when the microelectrode signal is played over a loudspeaker, and an abrupt change in microelectrode impedance. The 3D reconstructed positions of two such collision events are shown in Fig. 8, overlaid on corresponding MR images. The X-ray-determined locations of these collisions on the MR are very near to the ventral edge of the cortical tissue, consistent with the expected collision tissue location.

GRAY/WHITE MATTER TRANSITIONS. To further test our system *in vivo*, we assigned each recording site to gray matter, white matter, or sulcus using X-ray position estimates coregistered to

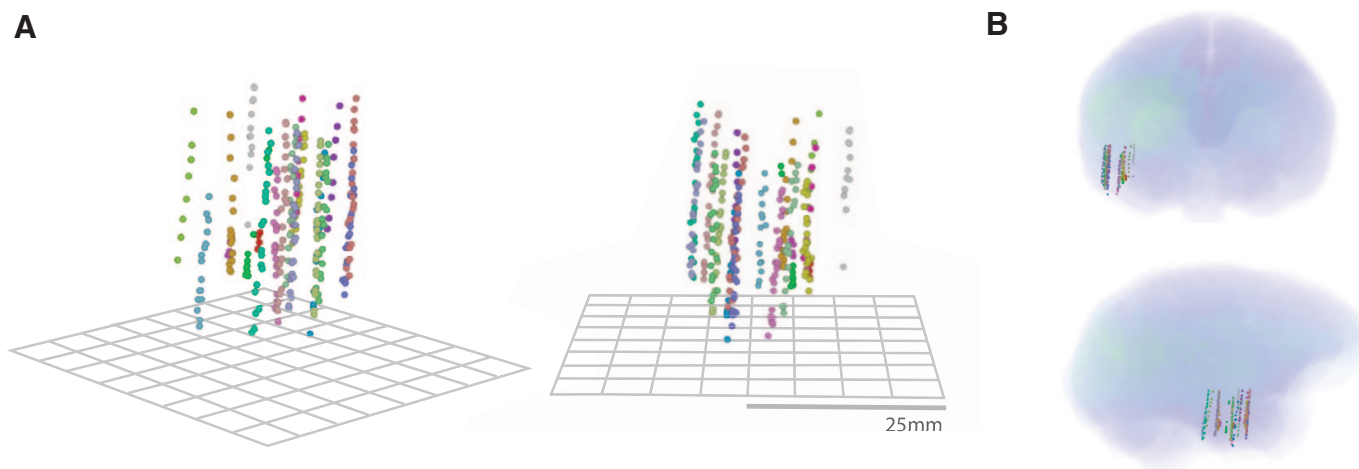


FIG. 6. A: two views of coregistered microelectrode recording sites from 20 sessions in the temporal lobe of one monkey (each dot represents one of 228 recording sites). Sites measured along each microelectrode penetration are plotted in the same color, but all sites were determined independently. B: the same data presented with a volume-rendered structural MRI volume overlaid, to provide anatomical bearings.

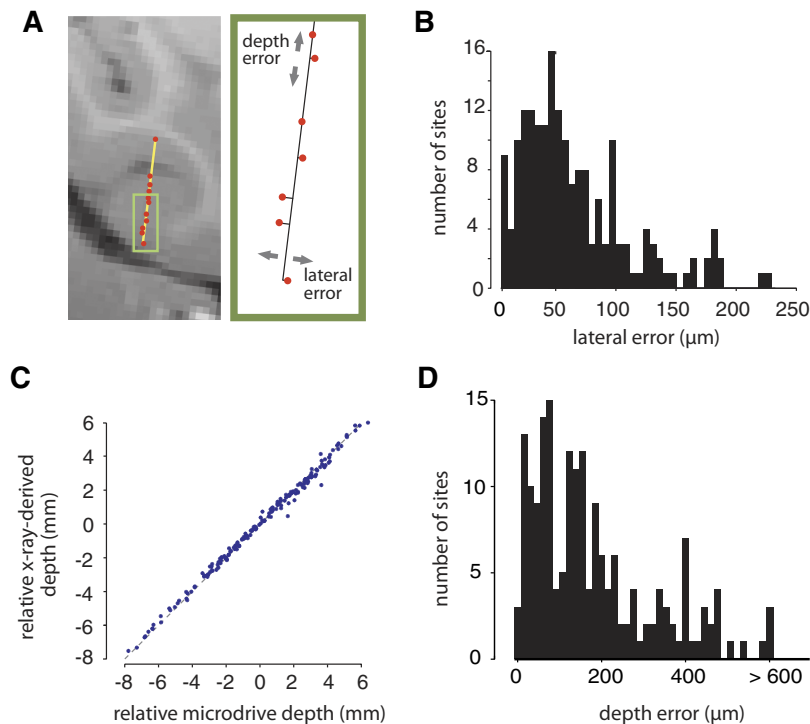


FIG. 7. Analysis of microelectrode movement in vivo. *A*: a collection of recording sites from an example microelectrode penetration. In general, since the microelectrode travels along a relatively straight path, 3D position estimates of serially collected recording sites along each microelectrode penetration were quite well fit by a straight line in 3D space. Red dots indicate recording sites, overlaid on a coregistered MRI slice that was selected to lie along the line fit (yellow line) for this penetration. The inset to the right shows an enlargement of a portion of the microelectrode track, without the MRI underlay, to illustrate how deviations from the line fit are decomposed into lateral and depth error. *B*: distribution of lateral errors from the line fits (absolute 3D distance normal to the line) for all recording sites ($n = 228$). Median lateral deviation was 52.7 μm , with 95% of measurements having errors <177.3 μm . *C*: a comparison of X-ray-derived depth estimates (ordinate) with microdrive-derived depth measurements (abscissa). For both X-ray-derived and microdrive measurements, the mean depth has been removed (i.e., zero represents the center of each microelectrode penetration) and the data from all microelectrode penetrations are overlaid. In general, X-ray-derived depth estimates were in good agreement with microdrive-derived values. *D*: a histogram of depth errors. The median absolute depth error was 136.2 μm and 95% of errors <481.3 μm . Although the system's depth accuracy is not as good as its lateral accuracy, in actual use, microdrive depth estimates can be used to supplement X-ray-derived estimates, allowing higher levels of accuracy.

structural MRI images of the same animal's brain (see METHODS). We then compared these tissue assignments to observed "multiunit activity" (voltage deviations above a fixed threshold; see METHODS) at each recording site, under the rationale that higher neuronal firing rates should be observed in gray matter, compared with white matter or the space within a sulcus, and that the transition across tissue types should be pronounced. The animal passively viewed six categories of objects rapidly presented on a monitor while voltage events were recorded: the "best" object category (evoking the largest mean number of events) was determined using half of the data and the response to that category was determined using the remainder of the data (i.e., an unbiased visually evoked response measure). Figure 9A shows an example MR-coregis-

tered recording track, with the response at each site represented by the area of the circle at each location. The magnitude of multiunit responses is in good agreement with anatomy, with larger responses in gray matter and smaller "responses" in white matter (we do not claim to be recording neuronal spikes in white matter because multiunit recordings do not differentiate well-isolated neurons from other background "events," including noise). To quantify this agreement across all recording sites, all gray-white and gray-sulcus boundaries were manually located along each microelectrode track. Each recording site was then accordingly assigned to a tissue type (gray, white, or sulcus) and assigned a distance from the nearest tissue boundary. All recording sites in gray and white matter were then aligned according to these distances, with positive values corresponding to positions on the gray-matter side of the boundary and negative values corresponding to position on the white-matter side of the boundary. The spatial median of these best visually evoked response magnitudes within a 1-mm sliding window across the gray-white boundary is plotted in Fig. 9B. Consistent with known properties of each tissue type, evoked "responses" are low in white matter, rising sharply as the boundary into gray matter is crossed. T1-weighted MR intensity values are plotted on the same axis for comparison (higher intensities for white matter than gray matter). Consistent with good alignment of recording sites with underlying anatomy, the profile of the evoked-response magnitude across the gray-white boundary and the T1-weighted signal intensity are strongly anticorrelated ($r = -0.93$).

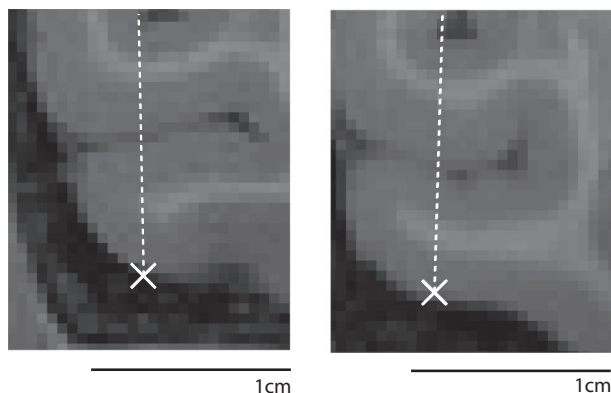


FIG. 8. Dura/bone collision sites. At the end of a few sessions (in a second animal), the microelectrode was purposely driven beyond audibly active cortex, into the dura mater and bone underlying the ventral surface of the brain, damaging the electrode tip. Dashed line indicates approximate electrode travel path (based on previous X-ray-reconstructed sites), and white 'X's indicate the 3D reconstructed position of the microelectrode tip when the microelectrode was confirmed broken (by listening to the recorded signal on an audio monitor and by monitoring microelectrode impedance).

DISCUSSION

We have demonstrated a highly accurate stereo X-ray system that can be used to routinely localize each and every recording site over the course of a standard electrophysiology experiment, combining the single-unit specificity of microelec-

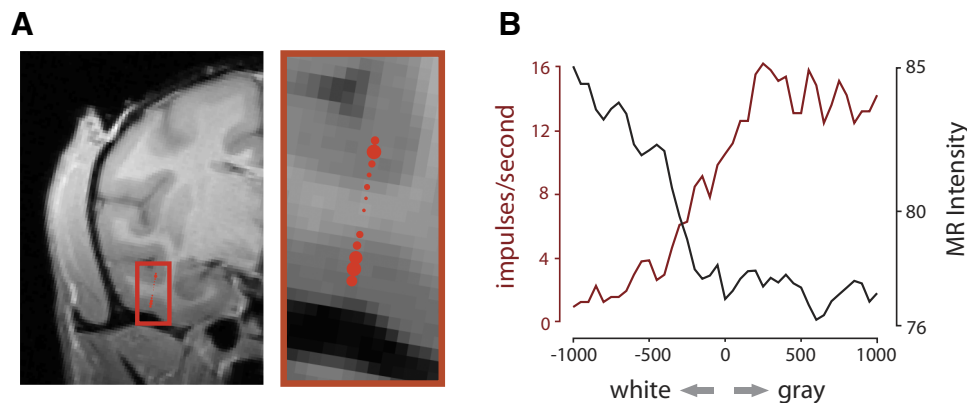


FIG. 9. Comparison of X-ray localized physiological activity with MRI-derived anatomy. *A*: an example microelectrode penetration into inferior temporal cortex. Red dots correspond to the stereo X-ray-resolved locations of recording sites during a recording session. The region within the red box is magnified for greater clarity. Dot area is proportional to visually evoked multiunit response magnitude. Consistent with anatomy, responses are large in gray matter and negligible in white matter. *B*: aligned gray-white boundaries for all recording sites. Gray-white boundaries were manually located along each X-ray/MRI coregistered microelectrode track. The distance from each recording site to the nearest gray-white boundary was measured, and all recording sites were aligned with negative distances indicating white matter, positive values indicating gray matter, and zero indicating the boundary itself. Median visually evoked multiunit responses ("impulses/s") within a 1-mm sliding window is plotted across this boundary (red line, left ordinate axis). Responses were recorded while the animal passively viewed visual stimuli belonging to 6 categories; the values plotted here constitute the response to the "best" category (e.g., the one evoking the largest response; assignment of "best" category was computed using half of the data, and the response was computed using the remainder of data). Consistent with good alignment with anatomy, small responses are observed in white-matter-labeled sites, rapidly increasing to large evoked responses on the gray side of the boundary. Mean T1-weighted MR intensity is plotted across the same boundary (black line, right ordinate axis) for comparison, showing white matter (high intensity) and gray matter (low intensity). As expected, evoked responses and T1-weighted signal intensity are strongly anticorrelated ($r = -0.93$).

trode recording with the spatial-mapping abilities of 3D imaging. The result is a spatially resolved map of individual single-unit response properties that can be measured deep within the brain, where the accuracy of traditional microelectrode mapping techniques normally breaks down.

The technique described here substantially extends previous work (Nahm et al. 1994). In contrast to many previously described microelectrode localization techniques (see INTRODUCTION), the method described here is practical for many neurophysiology laboratories, can be deployed on a day-to-day basis, and is minimally intrusive to ongoing experiments. Indeed, the required X-ray images can easily be acquired in a few seconds while a recording session is in progress. Each microelectrode recording site can be individually localized, rather than relying on a single measurement per day, resulting in a fuller picture of each recording session. Also, given that awake electrophysiology is already a highly demanding experimental technique, the relatively small incremental effort required by this technique does not present a substantial additional burden and can be added as a general matter of course. Furthermore, since this technique develops a detailed 3D map of recording sites in vivo and on-line, one does not need to wait for an animal to be euthanized to verify recording sites, and one can "course correct" midstudy to ensure that a given region is properly targeted or sampled with appropriate uniformity.

One immediate application of our technique is in the comparison of electrophysiological data with other measurements of brain activity, such as functional MRI. In particular, given the increasing popularity of fMRI in nonhuman primates, there is an increased demand to reconcile this relatively new technique with traditional direct measures of neuronal activity using microelectrodes. By allowing microelectrode recording locations to be mapped relative to an MR image, spatially resolved single- and multiunit recordings (and local field potentials) can be directly compared with fMRI activity at comparable positions. Such comparisons hold the potential to

resolve important outstanding issues in our understanding of how fMRI activity relates to underlying neuronal activity.

More broadly, our technique enables an entirely new kind of maps of neuronal activity to be collected. By collecting large numbers of spatially resolved microelectrode recordings, one can build up highly detailed 3D maps of brain activity with single-unit response specificity. Such maps have the power to reveal details of cortical microstructure (e.g., columns, laminar differences) even in deep brain regions where such structures are currently very difficult or impossible to measure. Knowledge of the fine-scale organization of cells within such brain regions, in turn, has the potential to reveal important insights into their function. It should also be noted that the technique described here need not be limited to recording microelectrodes—stimulating electrodes, electrodes for measuring chemical properties, as well as a variety of other invasive devices, such as cannulae (e.g., for drug delivery/measurement, viral vector delivery, etc.) and fiber optics (e.g., for measuring or perturbing neuronal activity with light) could all be localized using this technique.

Future directions

Although the system as instantiated in this study has key features that make it practical and relatively easy to use (see above), and it already has accuracies that compare favorably to those of other techniques, we see several open avenues for improvement.

In terms of accuracy improvement, we first note that, although we here used microdrive readings as an independent measure of accuracy (see RESULTS), in practice, microdrive data can easily be recorded alongside X-ray measurements, and these two data sources can be combined for even greater accuracy. In such a scenario, X-ray data would be used to determine a line fit for the path of the electrode and microdrive depth measurements would then be projected onto this line.

Such combined data are particularly useful, since each source of data complements the other. Although microdrives provide no information about the direction in which the microelectrode is tracking, they nonetheless produce highly accurate estimates of distance traveled along that track. Likewise, although the X-ray–derived estimates are somewhat weaker in estimating depths (Fig. 7), they are exquisitely accurate for estimating microelectrode track direction. Although it is not possible from our data to measure directly how much such an integration would improve accuracy, simple simulations of the electrode path line-fitting procedure (assuming 1- μ m error in microdrive measurements and X-ray *lateral* and *depth* errors of the magnitude demonstrated earlier) suggest that a threefold improvement in overall position accuracy should be possible.

Second, since image quality around the microelectrode tip is an important determinant of overall system accuracy *in vivo*, any refinement of this technique that improves image contrast should also improve localization accuracy. Perhaps the most obvious candidates for such improvement are the X-ray sources and X-ray detectors. Microfocal sources are currently available with twice the X-ray flux (2-mA current) and a smaller focal spot size (25 μ m) compared with the sources used here, which would result in higher image contrast and sharpness, even with shorter imaging time (less chance of motion blur) and more source filtration (for improved animal safety). Given that low image contrast in regions with dense skull interference is a major source of error in the results presented here, we believe that higher flux, in particular, could lead to substantial improvement in accuracy. Likewise, the use of more sensitive X-ray detectors could improve estimates of the microelectrode tip position. Another, related approach would be to enhance the estimate of the microelectrode tip location. For instance, it should be possible to mark microelectrodes at a known distance (e.g., a few millimeters) from their tips (e.g., a notch, bead, or some other feature could be affixed to or scored into the microelectrode shaft). It would then be possible to 3D localize this easier-to-localize feature and then to compute where the tip is relative to that feature (i.e., short distance extrapolation). Along a similar vein, general improvements in software image processing (e.g., filtering) have the potential to improve system accuracy.

Third, tissue distortion is another important factor limiting effective system resolution. Since we are ultimately interested in mapping tissue properties (e.g., neuronal activity), distortion of tissue (e.g., compression as the microelectrode advances) will lead to errors in the tissue-relative 3D maps produced by our technique. Since relatively little quantitative data are available concerning the mechanical behavior of brain tissue during microelectrode recording, it is difficult to know to what extent such compression affects our maps. One way to both study and potentially overcome this limitation would be to implant small fiducial markers “floating” within the brain tissue. Just as chronically implanted flexible microwires are thought to move with brain pulsations (providing more resilient cell isolations; e.g., Porada et al. 2000), small, biocompatible metal fiducial spheres could be embedded in brain tissue such that they provide a marker of brain movement as a microelectrode is advanced. In addition to providing data on the mechanical properties of brain tissue *in vivo* such fiducial spheres could also potentially serve as an elastic frame of reference that is resilient to tissue distortion (because the frame of

reference moves with the tissue). The development of such “internal” reference frames is an area of ongoing research within our laboratory.

Going forward, it will be important to provide even further benchmarks on the accuracy of this system. This is challenging in part because the accuracy we have achieved exceeds the 3D accuracy of readily available methods (e.g., microlesions). At the time of writing, the animals used here are still part of ongoing studies, so we were not able to show a comparison of this technique with histological analysis of microlesions. However, it should be noted that information gleaned from such a comparison is somewhat limited. It is generally not possible to generate accurate 3D reconstructions of brain tissue from histology, due to tissue shrinkage and distortion and due to the nontrivial nature of lining up serial brain slices. One area where microlesion histology does excel, however, is in determining electrode position relative to cortical layer. Assessing the suitability of this technique for estimating the cortical layer of particular recording sites (using either pure X-ray measurements or X-ray plus microdrive) will be an important and interesting future direction.

In terms of further improvements in ease of use, we envision improvements to both the hardware and software that will further enhance the robustness and practicality of this system. On the hardware side, the construction of gantries suitable for holding the sources and detectors in a larger number of configurations is possible and would allow flexible adaptation to the particulars of one’s experimental setup and physical constraints. Electronics for full software control of sources and detectors (power, shutter, acquire, safety, etc.) is straightforward and now in place in our laboratory. Fully integrated software for managing calibration, workflow, automated object (fiducial and microelectrode) segmentation, and results visualization is also relatively straightforward. Together these improvements yield a system that is easy-to-use and, whenever the user desires it, produces a high-accuracy, “on-line” electrode 3D localization result in a matter of seconds.

ACKNOWLEDGMENTS

We thank J. Deutsch, M. Maloof, L. Mariano, N. Pinto, and R. Marini for technical assistance and N. Li, and N. Majaj for comments on drafts of this work.

GRANTS

This work was supported in part by The Defense Advanced Research Projects Agency, The Pew Charitable Trusts, and The McGovern Institute for Brain Research. D. D. Cox was supported by a National Defense Science and Engineering Graduate Fellowship and a Rowland Junior Fellowship from Harvard University.

REFERENCES

- Bashore T. Fundamentals of X-ray imaging and radiation safety. *Catheter Cardiovasc Interv* 54: 126–135, 2001.
- Clarke SH, Southwood TRE. Risks from ionizing radiation. *Nature* 338: 197–198, 1989.
- DiCarlo JJ, Lane JW, Hsiao SS, Johnson KO. Marking microelectrode penetrations with fluorescent dyes. *J Neurosci Methods* 64: 75–81, 1996.
- Fung SH, Burstein D, Born RT. In vivo microelectrode track reconstruction using magnetic resonance imaging. *J Neurosci Methods* 80: 215–224, 1998.
- Glimcher PW, Ciaramitaro VM, Platt ML, Bayer HM, Brown MA, Handel A. Application of neurosonography to experimental physiology. *J Neurosci Methods* 108: 131–144, 2001.
- Kreiman G, Hung CP, Kraskov A, Quiroga RQ, Poggio T, DiCarlo JJ. Object selectivity of local field potentials and spikes in the macaque inferior temporal cortex. *Neuron* 49: 433–445, 2006.
- Matsui T, Koyano KW, Koyama M, Nakahara K, Takeda M, Ohashi Y, Naya Y, Miyashita Y. MRI-based localization of electrophysiological

- recording sites within the cerebral cortex at single-voxel accuracy. *Nat Methods* 4: 161–168, 2007.
- Nahm FK, Dale AM, Albright TD, Amaral DG.** In vivo microelectrode localization in the brain of the alert monkey: a combined radiographic and magnetic resonance imaging approach. *Exp Brain Res* 98: 401–411, 1994.
- Naselaris T, Merchant H, Amirkian B, Georgopoulos AP.** Spatial reconstruction of trajectories of an array of recording microelectrodes. *J Neurophysiol* 93: 2318–2330, 2005.
- Op de Beeck HP, Deutsch JA, Vanduffel W, Kanwisher NG, DiCarlo JJ.** A stable topography of selectivity for unfamiliar shape classes in monkey inferior temporal cortex. *Cereb Cortex* 18: 1676–1694, 2008.
- Porada I, Bondar I, Spatz WB, Kruger J.** Rabbit and monkey visual cortex: more than a year of recording with up to 64 microelectrodes. *J Neurosci Methods* 95: 13–28, 2000.
- Snodderly DM, Gur M.** Organization of striate cortex of alert, trained monkeys (*Macaca fascicularis*): ongoing activity, stimulus selectivity, and widths of receptive field activating regions. *J Neurophysiol* 74: 2100–2125, 1995.
- Valstar ER, Nelissen RGHH, Reiber JHC, Rozing M.** The use of Roentgen stereophotogrammetry to study micromotion of orthopaedic implants. *Photogram Remote Sens* 56: 376–389, 2002.
- Vlietstra RE, Wagner LK, Koenig T, Mettle F.** Radiation burns as a severe complication of fluoroscopically guided cardiological interventions. *J Interv Cardiol* 17: 131–142, 2004.
- Zoccolan D, Cox DD, DiCarlo JJ.** Multiple object response normalization in monkey inferotemporal cortex. *J Neurosci* 25: 8150–8164, 2005.